aligned value of 3.5 μ_B per Mn. It is also possible that this region may be a ferromagnetic phase on top of a separate non-ferromagnetic, charge-ordered phase. If so, the charge-ordered phase would have to be less than 2 nm (about two unit cells parallel to the **b** axis) thick to produce a magnetization within the error limits quoted. Such a thin region is unlikely, because the region of interest is very bright in the dark-field image (Fig. 2b), indicating that charge order is well established here. We have also taken a number of Fresnel images and diffraction patterns from other areas of the sample, and have seen magnetic domain walls and charge ordering in the same region (Supplementary Fig. II), which is further evidence for this unexpected phase.

In tilting the sample, we found that charge-ordered reflections perpendicular to a systematic row were far stronger for those parallel to the systematic row. Figure 2d shows a systematic row from the same region as Fig. 2c with strong charge-ordered reflections perpendicular to the row. This is strong evidence that charge order is predominantly a transverse modulation of the atoms, as discussed in ref. 11 based on evidence from neutron powder diffraction.

Using electron microscopy, we have shown that at 90 K, $La_{0.5}Ca_{0.5}MnO_3$ forms an inhomogeneous mixture of ferromagnetic and zero-moment (presumably antiferromagnetic[1]) regions. Each region extends for several micrometres, and can span several crystallographic grains. Our results suggest that charge order occurs not only in regions with no net magnetization, but can also occur in ferromagnetic regions. Very recently, evidence has been published[19] that is consistent with the possibility of a similar coexistence in $La_{0.25}Pr_{0.375}Ca_{0.375}MnO_3$. This charge-ordered, ferromagnetic phase is not predicted by conventional models[8–10], but unexpected phases such as this can arise from a simple hamiltonian[20].

We suggest that the bandgap that opens up below the charge-ordering transition temperature can be small enough that the valence electrons still have enough mobility to promote ferromagnetism via double exchange, and yet large enough to produce a charge density wave. This seems reasonable, as ferromagnetic coupling in the manganites should only require nearest-neighbour hopping. Furthermore, some degree of charge ordering may even be possible deep within the ferromagnetic regime, as diffuse charge-ordered reflections have been observed[21] in $La_{2/3}Ca_{1/3}MnO_3$. We further suggest that the bandgap is locally modified by strain within each grain, and that this results in the rich variety of phases that can coexist in the manganites. This may also explain the strong dependence of $La_{0.5}Ca_{0.5}MnO_3$ properties on grain size[5]. Therefore manganite phase diagrams based on composition alone paint an inadequate picture of manganite physics, and miss the richness and complexity that we have demonstrated here. □

1. Cheong, S.-W. & Hwang, H. Y. *Colossal Magnetoresistive Oxides* Monographs in Condensed Matter Science, Ch. 7 (ed. Tokura, Y.) (Gordon & Breach, Reading, UK, 2000).
2. Moreo, A., Yunoki, S. & Dagotto, E. Phase separation scenario for manganese oxides and related materials. *Science* **283**, 2034–2040 (1999).
3. Mathur, N. D. & Littlewood, P. B. The self-organised phases of manganites. *Solid State Commun.* **119**, 271–280 (2001).
4. Uehara, M., Mori, S., Chen, C. H. & Cheong, S.-W. Percolative phase separation underlies colossal magnetoresistance in mixed valent manganites. *Nature* **399**, 560–563 (1999).
5. Levy, P. *et al.* Controlled phase separation in $La_{0.5}Ca_{0.5}MnO_3$. *Phys. Rev. B* **62**, 6437–6441 (2000).
6. Radaelli, P. G., Cox, D. E., Capogna, L., Cheong, S.-W. & Marezio, M. Wigner-crystal and bi-stripe models for the magnetic and crystallographic superstructures of $La_{0.333}Ca_{0.667}MnO_3$. *Phys. Rev. B* **59**, 14440–14450 (1999).
7. Roy, M., Mitchell, J. F., Ramirez, A. P. & Schiffer, P. Doping-induced transition from double exchange to charge order in $La_{1-x}Ca_xMnO_3$ near x = 0.5. *Phys. Rev. B* **58**, 5185–5188 (1998).
8. Goodenough, J. B. Theory of the role of covalence in the perovskite type manganites [La,M(II)]MnO₃. *Phys. Rev.* **100**, 564–573 (1955).
9. De Gennes, P.-G. Effects of double exchange in magnetic crystals. *Phys. Rev.* **118**, 141–154 (1960).
10. Zener, C. Interaction between the d shells in the transition metals. II. Ferromagnetic compounds of manganese with perovskite structure. *Phys. Rev.* **82**, 403–405 (1951).
11. Radaelli, P. G., Cox, D., Marezio, M. & Cheong, S.-W. Charge, orbital and magnetic ordering in $La_{0.5}Ca_{0.5}MnO_3$. *Phys. Rev B* **55**, 3015–3023 (1997).
12. Mori, S., Chen, C. H. & Cheong, S.-W. Pairing of charge-ordered stripes in (La,Ca)MnO₃. *Nature* **392**, 473–476 (1998).
13. Chen, C. H., Cheong, S.-W. & Hwang, H. Y. Charge-ordered stripes in $La_{1-x}Ca_xMnO_3$ with x > 0.5. *J. Appl. Phys.* **81**, 4326–4330 (1997).
14. Hirsh, P., Howie, A., Nicholson, R., Pashley, D. W. & Whelan, M. J. *Electron Microscopy of Thin Crystals*, 2nd edn (Krieger, Malabar, Florida, 1977).
15. Lloyd, S. J., Mathur, N. D., Loudon, J. C. & Midgley, P. A. Magnetic domain wall width in $La_{0.7}Ca_{0.3}MnO_3$ thin films using Fresnel imaging. *Phys. Rev. B* **64**, 172407 (2001).
16. Dunin-Borkowski, R. E., McCartney, M. R, Smith, D. J. & Parkin, S. S. P. Towards quantitative electron holography of magnetic thin films using in-situ magnetization reversal. *Ultramicroscopy* **74**, 61–73 (1998).
17. Rez, D., Rez, P. & Grant, I. Dirac-Fock calculations of x-ray scattering factors and contributions to the mean inner potential for electron scattering. *Acta Crystallogr. A* **50**, 481–497 (1994).
18. Suzuki, Y. *et al.* Magnetic anisotropy of doped manganite thin films and crystals. *J. Appl. Phys.* **83**, 7064–7066 (1998).
19. Mori, S., Asaka, T. & Matsui, Y. Observation of magnetic domain structure in phase-separated manganites by Lorentz electron microscopy. *J. Electron Microsc.* **51**, 225–229 (2002).
20. Yunoki, S., Hotta, T. & Dagotto, E. Ferromagnetic A-type, and charge-ordered CE-type states in doped manganites using Jahn-Teller phonons. *Phys. Rev. Lett.* **84**, 3714–3717 (2000).
21. Zuo, J. M. & Tao, J. Nanometer-sized regions of charge ordering and charge melting in $La_{2/3}Ca_{1/3}MnO_3$ revealed by electron microdiffraction. *Phys. Rev. B* **63**, 060407 (2001).

....

Electroluminescence from single monolayers of nanocrystals in molecular organic devices

Seth Coe*†, **Wing-Keung Woo**†‡, **Moungi Bawendi**‡ & **Vladimir Bulović***

* *Laboratory of Organic Optoelectronics, Department of Electrical Engineering and Computer Science,*
‡ *Center for Materials Science and Engineering, Department of Chemistry, Massachusetts Institute of Technology, Cambridge, Massachusetts 02139, USA*
† *These authors contributed equally to this work*

....

The integration of organic and inorganic materials at the nanometre scale into hybrid optoelectronic structures enables active devices[1–3] that combine the diversity of organic materials with the high-performance electronic and optical properties of inorganic nanocrystals[4]. The optimization of such hybrid devices ultimately depends upon the precise positioning of the functionally distinct materials. Previous studies[5,6] have already emphasized that this is a challenge, owing to the lack of well-developed nanometre-scale fabrication techniques. Here we demonstrate a hybrid light-emitting diode (LED) that combines the ease of processability of organic materials with the narrow-band, efficient luminescence of colloidal quantum dots[7] (QDs). To isolate the luminescence processes from charge conduction, we fabricate a quantum-dot LED (QD-LED) that contains only a single monolayer of QDs, sandwiched between two organic thin films. This is achieved by a method that uses material phase segregation between the QD aliphatic capping groups and the aromatic organic materials. In our devices, where QDs function exclusively as lumophores, we observe a 25-fold improvement in luminescence efficiency (1.6 cd A^{-1} at 2,000 cd m^{-2}) over the best previous QD-LED results[5]. The reproducibility and precision of our

phase-segregation approach suggests that this technique could be widely applicable to the fabrication of other hybrid organic/inorganic devices.

The development of solution-based synthetic routes for creating CdSe(ZnS) nanocrystal QDs[4] generated a material set that was continuously tunable, narrow-band, and an efficient emitter of saturated colour across the visible spectrum[7]. Solution photoluminescence quantum efficiencies of QDs can exceed 50% (ref. 8), and by controlling the QD diameter during synthesis, the peak emission wavelength can be tuned continuously from 470 nm to 630 nm. Colloidal QD solution samples can be routinely prepared with size distributions of less than 6% standard deviation, corresponding to a photoluminescence full-width at half-maximum (FWHM) of less than 30 nm. These desirable emissive properties, unmatched by any class of organic chromophores, motivated the creation of hybrid organic/inorganic LEDs containing QDs[1,5]. To date the demonstrated efficiencies of QD-LEDs are far below those of state of the art all-organic LED technology[9–11]. However, investigation into the fundamental limits of QD-LED performance reveals their potential to become a versatile technological platform for the creation of planar light emitters. All of this motivates our own work in redesigning hybrid device structures on the nanoscale, in the hope of creating QD-LEDs that have properties unattainable using only organic materials, and efficiencies that make them technologically viable.

To isolate the role of QDs in the LED luminescence process from their participation in charge conduction, we fabricate hybrid QD-LEDs containing only a single monolayer of QDs sandwiched between organic thin films. The organic layers transport charge carriers to the vicinity of the QD monolayer from which the luminescence originates. This is in contrast to previous studies that utilized QD multilayer films, of the order of 10–20 layers thick, which had the dual function of both transporting electrons and serving as the emissive layer[1,5,12]. Poor conduction through QD multilayers[13] led to an injected charge imbalance, and consequently the luminescence efficiency of these early devices never exceeded 0.10 cd A[-1]. Furthermore, a high density of pinhole defects in QD multilayers resulted in low device yields and inconsistent device performance. These technological shortcomings are avoided in structures that use only a single monolayer of QDs as the emissive layer. Indeed, high device yields and consistent LED performance are standard for devices described here.

Our basic device structures[14] are shown in Fig. 1 inset, along with a schematic drawing of a core–shell-type QD passivated with trioctylphosphine oxide (TOPO) and trioctylphosphine (TOP) caps. The QD monolayer and the hole-transporting N,N′-diphenyl-N,N′-bis(3-methylphenyl)-(1,1′-biphenyl)-4,4′-diamine (TPD) layer are deposited in a single spin-casting step. Although spin-casting is possible for molecular organics, and typical for organic polymers, it limits the viable organic hole-transporting materials to those that are highly soluble in solvents such as toluene, alkanes and chloroform, which are preferred for solvating TOPO/TOP-capped QD colloids. It is desirable to have organic solubility of the order of 10 mg ml^{-1} to allow for a large range of possible solution mixtures and film thicknesses. Additionally, it is necessary to use an organic hole-transporting material that phase-segregates from the TOPO/TOP-capped QDs during the spinning process. TPD in chloroform meets all of these criteria. The luminescence of TPD also has a significant spectral overlap with the absorption spectra of CdSe QDs of all sizes, allowing the possibility of efficient exciton energy transfer from TPD to QDs.

The QD concentration in TPD/QD solutions is optimized to form a complete single monolayer on top of the TPD film. This is crucial to the creation of LEDs that are both efficient and monochromatic. Atomic force microscopy (AFM) images in Fig. 2a and b show the result of spinning at 1/5 of the optimal concentration, and confirm that TPD and QDs phase-segregate during the spinning process, yielding a QD coverage of 21%. Figure 2c shows a complete

single QD monolayer like those used in devices I and II. Optical absorption measurements of these bilayers indicate that QDs make up 5–10 vol.% of our 40-nm-thick films, confirming that all of the QDs are accounted for by this self-assembled, phase-segregated monolayer. Further confirmation of the phase segregation process is shown in Fig. 2d, where after thermal evaporation of 5 nm of TPD onto the QD monolayer the TPD forms droplets rather than a planar thin film. Thicker organic overlayers can be planar, as in Fig. 2f, which shows the smooth surface of the 40-nm-thick tris-(8-hydroxyquinoline)aluminium (Alq$_3$) overlayer in device I.

The electroluminescence spectra of our QD-LEDs are shown in Fig. 1. Spectral peaks at wavelengths of 562 and 400 nm, and the broader shoulder centred at 530 nm, are attributed to emission from QDs, TPD and Alq$_3$, respectively. The dashed lines in Fig. 1a show the decomposition of the electroluminescence spectra into Alq$_3$, TPD and QD contributions, which we quantify in terms of an emission fraction (f_x).

The external quantum efficiency of device I exceeds $\eta = 0.4\%$ for a broad range of device luminances (from 5 to 2,000 cd m^{-2}), peaking at $\eta = 0.52\%$ at 10 mA cm^{-2} (Fig. 3). The brightness of 100 cd m^{-2} is achieved at current density $J = 5.3$ mA cm^{-2}, voltage $V = 6.1$ V, corresponding to a luminescence efficiency of 1.9 cd A^{-1}. At 125 mA cm^{-2}, the brightness of device I is 2,000 cd m^{-2}, which corresponds to 1.6 cd A^{-1}, and a 25-fold improvement over the best previously reported QD-LED result[5].

In device I, holes are injected from the indium tin oxide (ITO) contact into the TPD host matrix, and are transported towards the single QD monolayer. Similarly, electrons are injected from the Mg:Ag cathode into the Alq$_3$ and are transported to the QDs. Exciton generation on QDs occurs via two parallel processes: direct charge injection and exciton energy transfer from organic molecules. For direct charge injection, electrons may be trapped at the QDs owing to the relative energy alignment of the lowest unoccupied molecular orbital (LUMO) levels of TPD, Alq$_3$ and the QDs (see the energy diagram in Fig. 4). For these charged QDs the barrier
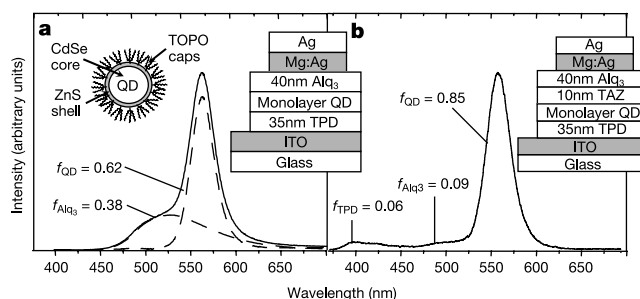

Figure 1 Electroluminescence spectra and structures for two QD-LEDs, devices I and II. Dashed lines, decomposition of spectra into Alq$_3$ (tris-(8-hydroxyquinoline)aluminium) and QD components. Inset, cartoon of a QD of the core–shell type. Solutions of coated QDs were prepared by the synthetic techniques of refs 4 and 7 with a photoluminescence efficiency of $22 \pm 2\%$. Absorption and luminescence spectra of our QD solutions peak at wavelengths of 545 and 561 nm, respectively, corresponding to a CdSe core diameter of ~38 Å coated with 1.5 monolayers of ZnS. The QDs are mixed into a chloroform solution of N,N′-diphenyl-N,N′-bis(3-methylphenyl)-(1,1′-biphenyl)-4,4′-diamine (TPD), which is then spin-cast onto clean, indium tin oxide (ITO) coated glass substrates. The QD and TPD concentrations are optimized such that spin-casting results in the formation of a single QD monolayer on top of a 35-nm-thick TPD layer. **a**, For device I, a 40-nm-thick film of Alq$_3$ is then thermally evaporated, followed by a 1-mm-diameter, 75-nm-thick Mg:Ag (10:1 by mass) cathode with a 50-nm Ag cap. **b**, For device II, a layer of 3-(4-biphenylyl)-4-phenyl-5-t-butylphenyl-1,2,4-triazole (TAZ) with a nominal thickness of 10 nm is evaporated before a 30-nm Alq$_3$ deposition. The spin-casting and device manipulation during growth is performed in a dry nitrogen environment, with moisture and oxygen content of less than 5 p.p.m. All measurements are done in air. For optimized growth conditions device yields are high, comparable to that of thermally evaporated all-organic LEDs. f, emission fraction.

to hole injection from the TPD is reduced. Upon acceptance of holes from TPD, excitons form on the QDs, and can subsequently recombine radiatively. Alternatively, excitons can be formed on organic molecules that are near grain boundaries, interstitial spaces, and voids in the single QD monolayer. These excitons can then undergo Förster energy transfer to the lower-energy QD sites, where they recombine radiatively.

Although we observed Förster energy transfer in photoluminescence studies of TPD/QD films, the current–voltage data of our QD-LED (Fig. 3 inset) also suggests generation of excitons on QDs via direct charge injection. Comparison of the current–voltage characteristics of device I with that of a control structure, without the monolayer of QDs, shows that QD-LEDs operate at a consistently higher voltage. The QD monolayer, therefore, inhibits charge conduction, which is consistent with charge-trapping on QD sites. For devices with a QD layer thicker than a single monolayer, the operating voltage increases further while the quantum efficiency is markedly reduced (not shown). This is consistent with the low efficiency and the high operating voltage measured in earlier studies that examined QD-LEDs containing more than ten layers of QDs. Indeed, studies of conduction through close-packed QD layers implicate charge-trapping as an important component of QD conduction[13,15]. In addition, devices that have only a partial monolayer of QDs have emission spectra that are dominated by Alq_3 (device I) or TPD (device II), indicating that precise control of the assembly of a QD monolayer is critical for optimal device operation.

Device II includes 10 nm of a material that blocks holes and excitons, 3-(4-biphenylyl)-4-phenyl-5-t-butylphenyl-1,2,4-triazole (TAZ), under the Alq_3 layer. The morphology of this layer, similarly guided by phase segregation (Fig. 2e), results in an incomplete coverage of 72%. The narrow emission spectrum in this device is due to the QDs (FWHM, 32 nm) with $f_{QD} = 0.85$. The device regions under TAZ voids have a similar structure to device I, and contribute to the observed Alq_3 emission ($f_{Alq3} = 0.09$). Elsewhere, TAZ suppresses Alq_3 emission by blocking transport of both holes and excitons into the Alq_3. The minimal TPD emission ($f_{TPD} = 0.06$) from this device is probably due to incomplete
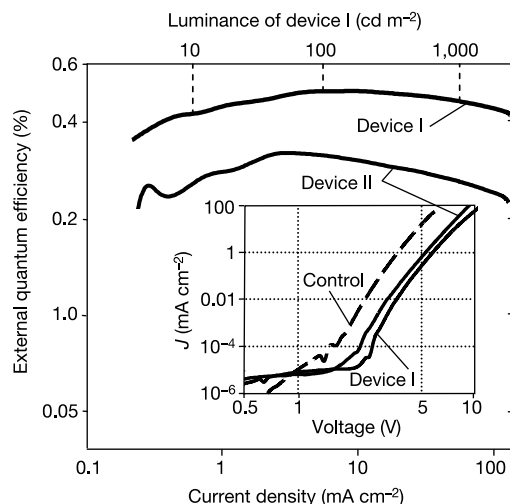

Figure 3 External quantum efficiency versus current density for the two devices shown in Fig. 1. The peak efficiency of device I is $\eta = 0.52\%$ at $10 \, mA \, cm^{-2}$ and 6.6 V, which corresponds to a luminance of $190 \, cd \, m^{-2}$. Inset, current density versus voltage data for the same devices, as well as for a control device that consists of spin-cast TPD and vacuum-deposited Alq_3 of the same thicknesses as used in device I. In all cases $J \propto V^9$ for $V > 3 \, V$, whereas the devices that contain QDs have operating voltages that are 15–30% greater than the control device.

exciton energy transfer from the TPD molecules to the QDs.

The fundamental limits of QD-LED performance are different from those of all-organic LEDs. The discrete energy structure of QDs gives rise to a narrow emission FWHM, which in our electroluminescence experiments is as small as 32 nm. In contrast, molecular organic LEDs have a typical FWHM of between 50 and 100 nm, although emission of some polymers and phosphorescent molecules was shown to be as narrow as 26 nm FWHM[16,17], but with long, low-energy tails. The vibrational structure of structurally flexible organics typically generates broad, single-molecule emis-
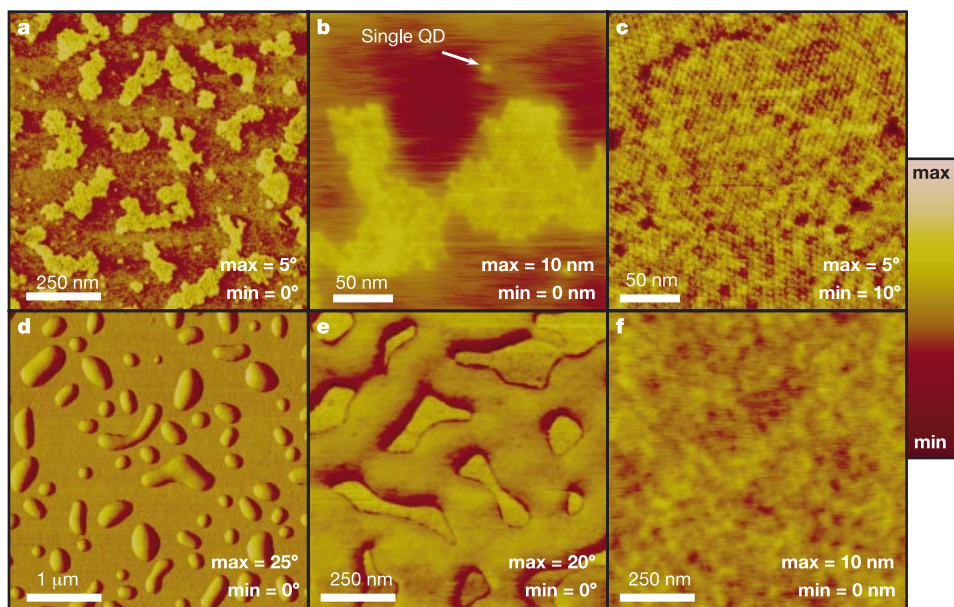

Figure 2 AFM images showing the surface morphology of various organic/QD films. **a**, Phase image of a partial monolayer of QDs on TPD after phase segregation during spin-coating. QD surface coverage is 21%. **b**, Height image of a close-up of **a**, showing both an island of QDs as well as individual QDs on a flat TPD background. **c**, Phase image of a complete, hexagonally packed monolayer of QDs phase segregated from the underlying TPD. Grain boundaries between ordered domains of QDs are observable. **d**, Phase image of TPD and QDs after thermal evaporation of a nominal 5 nm of TPD onto the complete QD layer of **c**. Material phase segregation results in TPD droplet formation. **e**, Phase image of nominal 10 nm of TAZ on surface similar to **c**. TAZ surface coverage is 72%. **f**, Height image of nominal 40 nm of Alq_3 on surface similar to **c**. Coverage is complete, with an r.m.s. surface roughness of 0.56 nm.
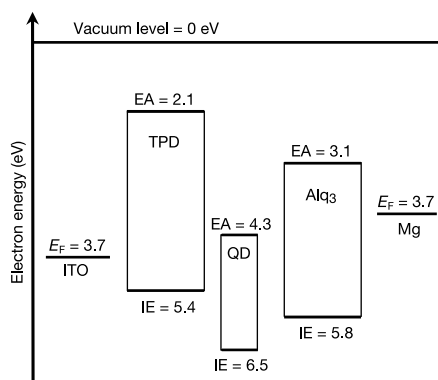
Figure 4 Proposed energy level diagram of device I. Values for ionization energy (IE) of all materials except QDs are taken from photoemission spectroscopy measurements[21]. Electron affinity levels (EA) were then calculated using optical absorption data. QD levels shown are from calculated values[12]. E_F, Fermi energy.

sion spectra at room temperature[18]. The same is not true of the rigid, covalently bonded inorganic QD, for which single-QD spectroscopy shows that the fundamental FWHM line width at room temperature is 14 nm (ref. 19) with a symmetrical, gaussian shape. It is the combination of spectral diffusion and size distribution of QDs in a sample that yields further line broadening. However, it is reasonable to expect that present-day techniques in QD preparation and processing could yield QD-LED line widths that are as narrow as 25 nm—which has already been accomplished in solution[20]. Such true colour saturation would benefit applications where efficient production of narrow-band light is desired. In particular, the creation of high-luminous-efficiency red and blue LEDs requires both high external quantum efficiency as well as narrow-band emission, to prevent the bulk of emission from occurring in the infrared or ultraviolet, respectively, where our eyes have minimal response.

We also note that the excited state of QDs mix the spin-triplet and spin-singlet exciton characteristics. In other material systems, the mixed states facilitate capture of both singlet and triplet excitons followed by rapid exciton recombination, leading to demonstrations of LEDs with nearly 100% internal quantum efficiency[9]. It remains an open question as to whether or not analogously efficient exciton harvesting is possible in QD-LEDs.

The present work shows that large area sheets of single QD monolayers ($>$cm^2) can be used in electrically active devices, minimizing QD material use to only the active region of the device. The phase segregation that governs formation of the organic/QD spin-cast thin film bilayers is a general fabrication process that we expect will be widely applicable. The process is governed by the physical size and chemical character of the two solvated constituents; the TPD molecules are small ($\sim$1 nm) and have aromatic character, whereas the QDs are comparatively large ($>$3 nm) and present a surface that consists of mostly alkane chains. In general, phase segregation is not limited to aromatic/aliphatic pairs, but governs the interaction between any pair of materials with disparate chemical functionality.

Although we have demonstrated a 25-fold improvement in the luminescent power efficiency over previously reported QD-LEDs, we believe that we have not reached the fundamental limits of device performance in terms of both quantum efficiency and colour saturation. □

1. Kagan, C. R., Mitzi, D. B. & Dimitrakopoulos, C. D. Organic-inorganic hybrid materials as semiconducting channels in thin-film field-effect transistors. *Science* **286**, 945–947 (1999).
2. Huynh, W. U., Dittmer, J. J. & Alivisatos, A. P. Hybrid nanorod-polymer solar cells. *Science* **295**, 2425–2427 (2002).
3. Colvin, V., Schlamp, M. & Alivisatos, A. Light-emitting diodes made from cadmium selenide nanocrystals and a semiconducting polymer. *Nature* **370**, 354–357 (1994).
4. Murray, C. B., Norris, D. J. & Bawendi, M. G. Synthesis and characterization of nearly monodisperse CdE (E = S, Se, Te) semiconductor nanocrystallites. *J. Am. Chem. Soc.* **115**, 8706–8715 (1993).
5. Schlamp, M. C., Peng, X. G. & Alivisatos, A. P. Improved efficiencies in light emitting diodes made with CdSe(CdS) core/shell type nanocrystals and a semiconducting polymer. *J. Appl. Phys.* **82**, 5837–5842 (1997).
6. Dabbousi, B. O., Bawendi, M. G., Onitsuka, O. & Rubner, M. F. Electroluminescence from CdSe quantum-dot/polymer composites. *Appl. Phys. Lett.* **66**, 1316–1318 (1995).
7. Dabbousi, B. O. *et al.* (CdSe)ZnS core-shell quantum dots: Synthesis and characterization of a size series of highly luminescent nanocrystallites. *J. Phys. Chem. B* **101**, 9463–9475 (1997).
8. Hines, M. A. & Guyot-Sionnest, P. Synthesis and characterization of strongly luminescing ZnS-capped CdSe nanocrystals. *J. Phys. Chem.* **100**, 468–471 (1996).
9. Adachi, C. *et al.* Nearly 100% internal phosphorescence efficiency in an organic light-emitting device. *J. Appl. Phys.* **90**, 5048–5051 (2001).
10. Moller, S. & Forrest, S. R. Improved light out-coupling in organic light emitting diodes employing ordered microlens arrays. *J. Appl. Phys.* **91**, 3324–3327 (2002).
11. Dirr, S., Bohler, A., Wiese, S., Johannes, H. H. & Kowalsky, W. Organic light emitting diodes with reduced spectral and spacial halfwidths. *Jpn J. Appl. Phys.1* **37**, 1457–1461 (1998).
12. Mattoussi, H. *et al.* Electroluminescence from heterostructures of poly(phenylene vinylene) and inorganic CdSe nanocrystals. *J. Appl. Phys.* **83**, 7965–7974 (1998).
13. Leatherdale, C. A. *et al.* Photoconductivity in CdSe quantum dot solids. *Phys. Rev. B* **62**, 2669–2680 (2000).
14. Era, M., Adachi, C., Tsutsui, T. & Saito, S. Double-heterostructure electroluminescent device with cyanine-dye bimolecular layer as an emitter. *Chem. Phys. Lett.* **178**, 488–490 (1991).
15. Morgan, N. Y. *et al.* Electronic transport in films of colloidal CdSe nanocrystals. *Phys. Rev. B* **66**, 075339 (2002).
16. Liu, J., Shi, Y. J. & Yang, Y. Improving the performance of polymer light-emitting diodes using polymer solid solutions. *Appl. Phys. Lett.* **79**, 578–580 (2001).
17. Kwong, R. C. *et al.* Efficient, saturated red organic light emitting devices based on phosphorescent platinum(II) porphyrins. *Chem. Mater.* **11**, 3709–3713 (1999).
18. Tamarat, P., Maali, A., Lounis, B. & Orrit, M. Ten years of single-molecule spectroscopy. *J. Phys. Chem. A* **104**, 1–16 (2000).
19. Empedocles, S. A., Norris, D. J. & Bawendi, M. G. Photoluminescence spectroscopy of single CdSe nanocrystallite quantum dots. *Phys. Rev. Lett.* **77**, 3873–3876 (1996).
20. Murray, C. B., Kagan, C. R. & Bawendi, M. G. Synthesis and characterization of monodisperse nanocrystals and close-packed nanocrystal assemblies. *Annu. Rev. Mater. Sci.* **30**, 545–610 (2000).
21. Hill, I. G. & Kahn, A. Organic semiconductor heterointerfaces containing bathocuproine. *J. Appl. Phys.* **86**, 4515–4519 (1999).

....

Metastable garnet in oceanic crust at the top of the lower mantle

Tomoaki Kubo*, **Eiji Ohtani***, **Tadashi Kondo***, **Takumi Kato**†, **Motomasa Toma***, **Tomofumi Hosoya***, **Asami Sano***, **Takumi Kikegawa**‡ **& Toshiro Nagase**§

* *Institute of Mineralogy, Petrology and Economic Geology, Graduate School of Science, Tohoku University, Sendai 980-8578, Japan*
† *Institute of Geoscience, University of Tsukuba, Tsukuba 305-8571, Japan*
‡ *Photon Factory, High Energy Accelerator Research Organization, Tsukuba 305-0801, Japan*
§ *The Tohoku University Museum, Sendai 980-8578, Japan*

As oceanic tectonic plates descend into the Earth's lower mantle, garnet (in the basaltic crust) and silicate spinel (in the underlying peridotite layer) each decompose to form silicate perovskite—the 'post-garnet' and 'post-spinel' transformations, respectively. Recent phase equilibrium studies[1,2] have shown that the post-garnet transformation occurs in the shallow lower mantle in a cold slab, rather than at $\sim$800 km depth as earlier studies indicated[3–6], with the implication that the subducted basaltic crust is unlikely to become buoyant enough to delaminate as it